

Optical Response, Lithium Doping, and Charge Transfer in Sn-Based 312 MAX Phases

Hadi, M. A., Kelaidis, N., Christopoulos, S., Chroneos, A., Naqib, S. H. & Islam, A. K. M. A

Published PDF deposited in Coventry University's Repository

Original citation:

Hadi, MA, Kelaidis, N, Christopoulos, S, Chroneos, A, Naqib, SH & Islam, AKMA 2023, 'Optical Response, Lithium Doping, and Charge Transfer in Sn-Based 312 MAX Phases', ACS Omega, vol. 8, no. 28, 3c03645, pp. 25601–25609.

<https://doi.org/10.1021/acsomega.3c03645>

DOI 10.1021/acsomega.3c03645

ESSN 2470-1343

Publisher: American Chemical Society

Copyright © 2023 The Authors. Published by American Chemical Society CC BY-NC-ND

Optical Response, Lithium Doping, and Charge Transfer in Sn-Based 312 MAX Phases

Md. Abdul Hadi,* Nicolas Kelaidis, Stavros-Richard G. Christopoulos, Alexander Chroneos, Saleh Hasan Naqib, and A. K. M. Azharul Islam



Cite This: *ACS Omega* 2023, 8, 25601–25609



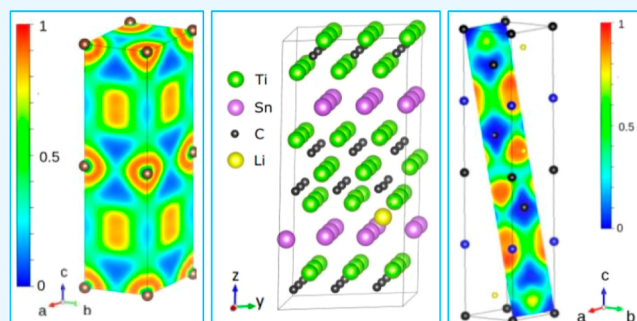
Read Online

ACCESS |

Metrics & More

Article Recommendations

ABSTRACT: The optical response, lithium doping, and charge transfer in three Sn-based existing M_3SnC_2 MAX phases with electron localization function (ELF) were investigated using density functional theory (DFT). Optical calculations show a slight optical anisotropy in the spectra of different optical parameters in some energy ranges of the incident photons. The peak height is mostly slightly higher for the polarization $\langle 001 \rangle$. The highest peak shifts toward higher energy when the M-element Ti is replaced by Zr and then by Hf. Optical conductivity, refractive index, extinction coefficient, and dielectric functions reveal the metallic nature of Ti_3SnC_2 , Zr_3SnC_2 , and Hf_3SnC_2 . The plasma frequencies of these materials are very similar for two different polarizations and are 12.97, 13.56, and 14.46 eV, respectively. The formation energies of Li-doped Zr_3SnC_2 and Hf_3SnC_2 are considerably lower than those of their Li-doped 211 MAX phase counterparts Zr_2SnC and Hf_2SnC . Consistently, the formation energy of Li-doped Ti_3SnC_2 is lower than that of the corresponding 2D MXene Ti_3C_2 , which is a promising photothermal material. The Bader charge is higher in magnitude than the Mulliken and Hirschfeld charges. The highest charge transfer occurs in Zr_3SnC_2 and the lowest charge transfer occurs in Ti_3SnC_2 . ELF reveals that the bonds between carbon and metal ions are strongly localized, whereas in the case of Sn and metal ions, there is less localization which is interpreted as a weak bond.



1. INTRODUCTION

MAX phases represent a family of ternary carbides, nitrides, and more recently borides with the chemical formula $M_{n+1}AX_n$ ($n = 1, 2, 3$).¹ In their chemical formulas, M is an early transition metal (Sc, Lu, Ti, V, Zr, Nb, Mo, Hf, Ta, Cr, and Mn), A is an A-group element (Al, Ga, In, Tl, Si, Ge, Sn, Pb, P, As, S, Se, and Te) or now any late transition metal (Fe, Cd, Zn, Ir, Cu, and Au), and X is C, N, or B.^{1–3} Depending on the layer index n , the MAX phases are classified into several sub-families, such as M_2AX (211), M_3AX_2 (312), and M_4AX_3 (413) phases for $n = 1, 2$, and 3, respectively.⁴ This family of compounds crystallizes in the hexagonal space group (no. 194) and consists of hexagonal $M_{n+1}X_n$ layers and planar A-atomic sheets along the c -direction.⁵ Atoms in $M_{n+1}X_n$ layers are covalently bonded, and these layers have a ceramic nature, whereas A-atomic sheets are metallic in nature. These metallic and ceramic layers and sheets alternately stack along the c -axis, and this arrangement is the key for the MAX phases' unusual combination of metallic and ceramic characteristics.⁶ As the layer index n increases, the ceramic layers in the unit cell of MAX phases are more numerous than the metallic sheets. In fact, a metallic sheet is separated by $(n + 1)$ ceramic layers as in the 211 MAX phases ($n = 1$), a metallic sheet is separated by

two ceramic layers. The metallic properties possessed by MAX phases are electrical and thermal conductivity, relative ductility and easy machinability, and resistance to thermal shock, damage tolerance, and plastic behavior at high temperatures.⁴ The ceramic properties that MAX phases possess are oxidation resistance, extreme refractoriness, elastic stiffness, low density, and good corrosion resistance.⁵

MAX-phases have become very attractive materials for various technological and engineering applications due to the combination of the above-mentioned properties. MAX phases have a wide range of applications, such as high-temperature operational materials, porous exhaust gas filters for automobiles, bond-coat layers in thermal barrier coating (TBC) systems, heat exchangers, coatings for electrical contacts, potential accident tolerant fuel claddings in third-generation light-water reactors, heating elements, wear- and corrosion-

Received: May 24, 2023

Accepted: June 20, 2023

Published: July 6, 2023



protective surface coatings, and solar receiver and storage tank in concentrated solar power units. Additionally, they have potential uses as electrodes, resistors, capacitors, biocompatible materials, rotary electrical equipment contacts, nozzles, and tools for die pressing and impact-resistant materials such as projectile-proof armors.^{4,7–11} In recent times, MAX phases have become prevalent for use in nuclear reactors as neutron radiation-resistant materials.¹² MAX phases have become popular in the production of their 2D derivative “MXene” for use as energy storage materials and electrodes in micro-supercapacitors, electrochemical capacitors, and batteries.¹³

Zhao et al.¹⁴ determined the interesting electrochemical performance of Nb₂SnC in Li-ion electrolytes, which has sparked great interest in the scientific community for Sn-containing MAX phases. Following this report, two Sn-based MAX phases were synthesized, and lithiation in the Sn-based 211 MAX phases was performed theoretically.^{15–17} Moreover, a set of theoretical studies have reported different physical properties of Sn-based MAX phases. The structural, electronic, mechanical and lattice dynamical properties of Sc₂SnC, including defect processes, in comparison to those of existing M₂SnC MAX phases are reported in a recent study.⁵ In another study, the V₂SnC MAX phase was predicted as a chemically stable, damage- and radiation-tolerant thermal barrier coating (TBC) material.¹⁸ The electronic structure, bonding nature, and defect processes in Sn-based 211 MAX phases Ti₂SnC, Nb₂SnC, Hf₂SnC, Zr₂SnC, and Lu₂SnC were reported in 2019.¹⁹ The mechanical behavior, lattice thermal conductivity, and vibrational properties of the Lu₂SnC MAX phase have also been investigated.²⁰

The 211 MAX family has a comparatively large number of Sn-based compounds, and more studies have been conducted on them. Conversely, there are only three Sn-based compounds in the 312 MAX family, and research conducted on them is also relatively less. Ti₃SnC₂ is the first Sn-containing compound in the 312 MAX phase family, synthesized in 2007.²¹ Zr₃SnC₂ and Hf₃SnC₂ were first predicted in 2014 and synthesized in 2017.²² A notable comprehensive theoretical work on three Sn-based compounds of the 312 MAX family was published in 2018.²³ This work included the mechanical, thermal, and electronic properties along with defect processes and theoretical Vickers hardness. The electron localization function (ELF), charge transfer, and optical response have not been extensively discussed for the Sn-based 312 MAX phases. Here, we aim to investigate these properties along with the formation energy of Li-doped systems using density functional theory (DFT).

2. COMPUTATIONAL APPROACHES

The CASTEP code²⁴ was the main DFT tool in this study. The Perdew–Burke–Ernzerhof (PBE) functional within the generalized gradient approximation (GGA)²⁵ was applied to evaluate the electronic exchange correlation potential. Generally, spin-polarization calculations using DFT + *U* need to be considered for compounds containing transition metals. All MAX phases contain transition metals. But, for MAX phases, it has been established that spin-polarization calculation is essential only for phases containing Mn, Cr, Ni, or Fe. These MAX phases are known as magnetic MAX phases. Previously, we calculated the spin-polarized band structure of Nb₂CuC and found no effect.²⁶ Therefore, here we avoided the spin-polarization based DFT + *U* calculations. The Vanderbilt type ultrasoft pseudopotential²⁷ was picked to

model the interaction between the electron and the ion core. A Γ -centered *k*-point mesh of a $17 \times 17 \times 2$ grid under the Monkhorst–Pack (MP) scheme²⁸ was used to integrate over the first Brillouin zone in the reciprocal space of a hexagonal unit cell of the compounds studied here. A plane-wave cutoff energy of 700 eV was applied in this study to expand the eigenfunctions of the valence and nearly valence electrons of atoms comprising the systems. The Broyden–Fletcher–Goldfarb–Shanno (BFGS) algorithm²⁹ was applied to minimize the total energy as well as the internal forces to optimize the geometry. The convergence tolerance for the total energy is set to 5×10^{-6} eV/atom, the maximum ionic Hellmann–Feynman force to 0.01 eV/Å, the maximum ionic displacement to 5×10^{-4} Å, and the maximum stress to 0.02 GPa. A supercell of $3 \times 3 \times 1$ size with 108 atoms was constructed for each phase for the calculation of formation energy of Li-doped systems, and the geometry of supercells was optimized using a plane-wave basis set cut-off energy of 450 eV and a Γ -centered *k*-point mesh of $3 \times 3 \times 2$ -grid in the MP scheme. ELF and Bader charge analysis were performed with the VASP code³⁰ under the optimization conditions used for optical and other calculations.

3. RESULTS AND DISCUSSIONS

3.1. Optical Properties. The interaction of a photon with an electron in a crystalline system can be described considering the time dependent perturbations of the ground state electronic states of the system. Now, CASTEP offers two methods for calculating optical properties; the first one is based on standard DFT Kohn–Sham orbitals and the other one is grounded on time-dependent DFT (TD-DFT) theory, which is more accurate but much more computationally intensive. Here, we performed standard DFT optical calculations. In this method the excited states are treated as unoccupied Kohn–Sham states. The transition between occupied and unoccupied states is caused by the photon’s electric field (the effect of the magnetic field is weakened by a factor of v/c). When these excitations are combined they are called plasmons, which are most easily observed by electrons passing rapidly through the system rather than photons, because transverse photons cannot excite longitudinal plasmons. Conversely, if the transitions are independent they are known as single particle excitations. The spectra arising from these excitations can be assumed to be the joint density of states between the valence and conduction bands, modeled by accurate matrix elements, as given by the selection rules associated with optical transitions.

Owing to the hexagonal crystal symmetry of the MAX compounds, the polarization direction $\langle 100 \rangle$ of the incident photon is at right angles to the direction of the associated electric field, and the polarization direction $\langle 001 \rangle$ is parallel to the crystallographic *c*-axis. As MAX materials are partially metallic, their intraband transitions have a momentous effect in the lower energy part (i.e., far infrared region) of the spectrum.^{31,32} CASTEP does not include intraband transitions by default to directly probe the optical properties of insulators and semiconductors. When calculating the optical properties of metallic compounds using CASTEP, the intraband contribution to the optical properties is ensured by including a semi-empirical Drude term in the optical conductivity through the plasma frequency ω_p and the damping parameter γ_D . The Drude damping parameter accounts for the spectral broadening as a result of electron–electron scattering (including the Auger process), electron-phonon scattering and electron-defect

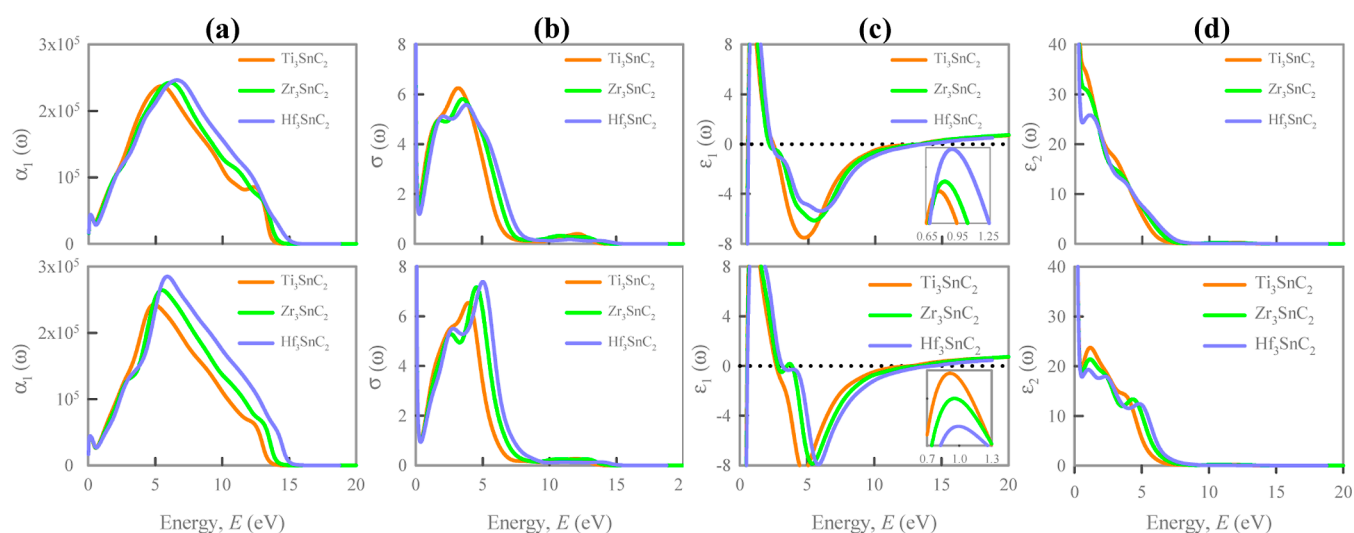


Figure 1. Optical properties of three Sn-based 312 MAX phases: (a) absorption coefficient, (b) optical conductivity, (c) real part of the dielectric function, and (d) imaginary part of the dielectric function. The upper panels are for the polarization $\langle 100 \rangle$ and the lower panels are for the polarization $\langle 001 \rangle$.

scattering. Usually, the plasma frequency, ω_p ranges from 2 to 10 eV and the Drude damping coefficient, γ_D varies from 0.02 to 0.08 eV for metallic crystals. For partially metallic MAX and MAX-like compounds, good results are obtained when the plasma frequency is chosen close to 3 and 0.05 eV is used as the Drude damping parameter.^{31–33} In this calculation, we therefore used 3 and 0.05 eV as the plasma frequency and Drude damping, respectively. Furthermore, in all optical property calculations we used 0.5 eV as Gaussian smearing for the metallic Sn-based 312 MAX phases.

The frequency-dependent complex dielectric function, $\epsilon(\omega) = \epsilon_1(\omega) + i\epsilon_2(\omega)$, consisting of a real, $\epsilon_1(\omega)$, and an imaginary part, $\epsilon_2(\omega)$, is a leading optical parameter. Among the two parts, the imaginary part, $\epsilon_2(\omega)$, leads to the calculation of the other optical parameters and can be expressed as

$$\epsilon_2(\omega) = \frac{2e^2\pi}{\Omega\epsilon_0} \sum_{k,v,c} |\langle \psi_k^c | \mathbf{u} \cdot \mathbf{r} | \psi_k^v \rangle|^2 \delta(E_k^c - E_k^v - E) \quad (1)$$

where ω refers to the photon frequency, e denotes the electronic charge, Ω defines the unit cell volume, \mathbf{u} is the unit vector parallel to the polarization direction of the incident electric field, and ψ_k^c and ψ_k^v stand for the wave functions linked to the conduction and valence band electrons at a specific k , respectively. The expressions for other optical functions such as reflectivity, refractive index, optical conductivity, absorption coefficient, and energy loss function can be derived from $\epsilon_2(\omega)$ and these expressions are available in the literature.^{17,34} All optical parameters of Sn-based 312 MAX phases are calculated using conventional unit cells for photon energies up to 20 eV.

Figure 1a shows the optical absorption coefficient $\alpha(\omega)$ as a function of photon energy. The upper panel exhibits $\alpha(\omega)$ for the polarization $\langle 100 \rangle$ and the lower panel for the polarization $\langle 001 \rangle$. Absorption coefficient $\alpha(\omega)$ is a measure of how far light of a specific wavelength will penetrate a material before it is completely absorbed. It also delivers information about optimal solar energy conversion efficiency. Notably, static absorption coefficients represent universal non-zero values for the M_3SnC_2 MAX phases studied here, as in other metallic hexagonal systems.^{17,35,36} The spectral features are slightly different for the two different polarizations and the peak

heights are slightly higher for the polarization $\langle 001 \rangle$. Up to 2.5 eV, the absorption rates for all three Sn-based 312 MAX phases are the same for both polarizations. Between 2.5 and 4.5 eV of photon energy, the absorption rate is the highest for Ti_3SnC_2 and lowest for Hf_3SnC_2 . The highest peak shifts toward higher energies when the M-element Ti is replaced by Zr and then by Hf. Above photon energies 6.1 and 5.3 eV, the absorption rates of light for Hf_3SnC_2 are the highest for the polarizations $\langle 100 \rangle$ and $\langle 001 \rangle$, respectively. In the energy range between 13.8 and 15.5 eV, the absorption rates of the three Sn-based MAX phases drop to zero for both polarizations.

Figure 1b shows the optical conductivity $\sigma(\omega)$ of three Sn-based 312 MAX phases as a function of incident photon energy. The upper panel exhibits $\sigma(\omega)$ for the polarization $\langle 100 \rangle$ and the lower panel for the polarization $\langle 001 \rangle$. Optical conductivity of a material is an essential optical parameter that indicates its electrical conductivity in the presence of an alternating electric field. This parameter is again a good predictor of the photoconductivity of a material.³⁷ A sharp peak in the spectra of optical conductivity due to both polarization directions in the region near the zero frequency (energy) indicates the metallic conductivity of the M_3SnC_2 MAX phases. As the photon energy increases, the optical conductivity spectrum shifts from the base of the sharp peak to another broad peak. The order of height of these broad peaks for the polarization $\langle 100 \rangle$ follows the order of Ti, Zr, and Hf in the periodic table. The opposite trend is observed for the polarization $\langle 001 \rangle$. In the lattice of MAX phases, the direction $[100]$ implies the basal “ ab ” planes, while the direction $[001]$ indicates the direction perpendicular to the basal planes. The carrier velocity in the basal plane is higher than that along the direction perpendicular to the basal plane. As the optical properties mainly depend on the electronic structure of the compound, the difference in carrier velocity in different directions may be the reason for optical anisotropy in the MAX phases under study. These peaks shift toward higher energies when the M-element Ti is replaced by Zr and then by Hf for both the polarizations. None of the compounds in the M_3SnC_2 family exhibit optical conductivity above 15 eV of photon energy.

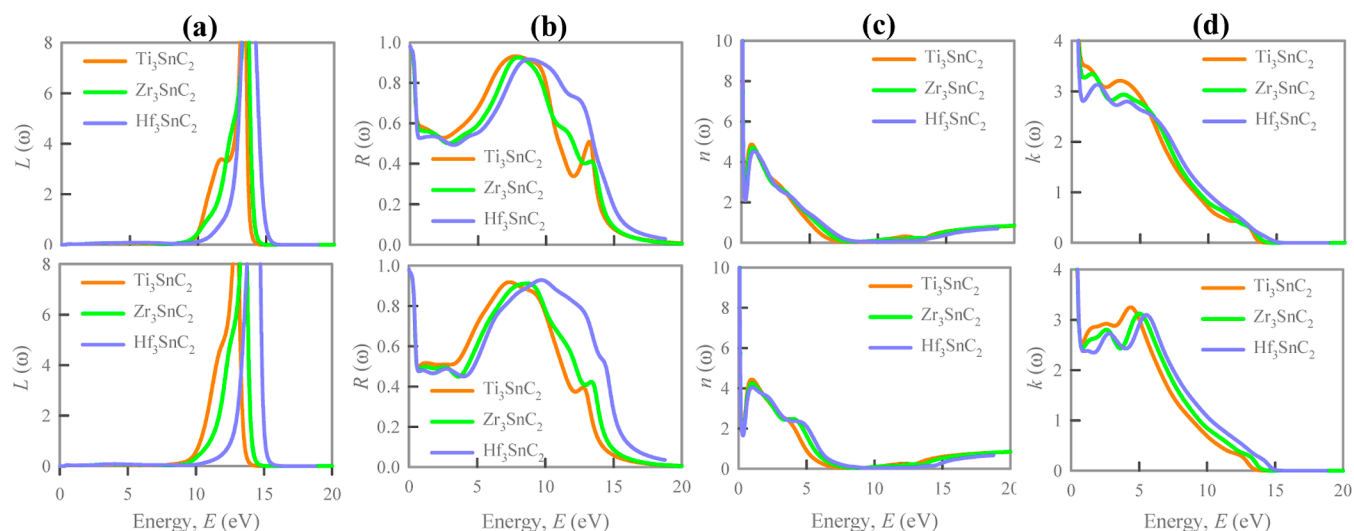


Figure 2. Optical properties of the three Sn-based 312 MAX phases: (a) energy loss function, (b) optical reflectivity, (c) refractive index, and (d) extinction coefficient. The upper panels are for the polarization $\langle 100 \rangle$ and the lower panels are for the polarization $\langle 001 \rangle$.

Figure 1c exhibits the real part, $\epsilon_1(\omega)$, of the dielectric function as a function of photon energy. The upper panel reveals $\epsilon_1(\omega)$ for the polarization $\langle 100 \rangle$ and the lower panel, for the polarization $\langle 001 \rangle$. The real part, $\epsilon_1(\omega)$, of the dielectric function represents the ability of the material to store electrical energy (electronic polarizability) or to allow an electric field to pass through it. In both panels, the large negative value of $\epsilon_1(\omega)$ in the low energy part of each spectrum reveals the Drude-like behavior of the Sn-based 312 MAX phases. Again, the real part $\epsilon_1(\omega)$ moves from negative to zero, indicating the metallic nature of these MAX compounds. The non-zero value of $\epsilon_1(\omega)$ indicates the possibility of large availability of free charge carriers in these metallic systems. For the polarization $\langle 100 \rangle$, all spectra reach their maximum peaks in the range of 0.75–0.89 eV of incident photon energy (refer to the inset of the figure). Within the above mentioned range of photon energies, the spectrum for Ti_3SnC_2 touches its highest peak at the lowest energy, and the spectrum for Hf_3SnC_2 arrives at the highest peak at the highest energy. The peak height is higher for Hf_3SnC_2 and lower for Ti_3SnC_2 . Spectral peak features are fairly different for the polarization $\langle 001 \rangle$. For this polarization, the highest peaks lie between 0.92 and 1.00 eV of incident photon energy (refer to the inset of the figure). The highest peak is seen for Ti_3SnC_2 and the lowest peak, for Hf_3SnC_2 . The spectra of $\epsilon_1(\omega)$ for both polarizations in the range of photon energies from 1.96 to 12.96 eV reveal negative values. The negative part of the real component of the dielectric constant simply states that the displacement field \mathbf{D} lags behind the electric field \mathbf{E} due to the inertia of the electrons. Materials with a negative value of $\epsilon_1(\omega)$ are of great technological importance for many applications, such as perfect (super) lens microwave circuits, antenna elements, optical switches and modulators. They essentially enable access to parts of the electromagnetic spectrum where conventional materials do not respond. Therefore, the three Sn-based 312 MAX phases studied here can be employed in these applications in a wide range of the solar spectrum (1.96 to 12.96 eV).

Figure 1d represents the imaginary part $\epsilon_2(\omega)$ of the dielectric function for the polarization $\langle 100 \rangle$ (upper panel) and $\langle 001 \rangle$ (lower panel). The part $\epsilon_2(\omega)$ is associated with

dielectric loss and is always positive and characterizes the loss factor or energy absorbed by a material per its unit volume. It actually indicates the ohmic resistance of the material. It also describes the ability of a material to enduringly absorb energy from a time-varying electric field. It approaches zero from above (positive value) for both polarizations, indicating the metallic nature of the Sn-based 312 MAX phases studied here. The spectra due to $\epsilon_2(\omega)$ exhibit a distinct anisotropic nature in the optical properties of MAX phases under consideration in the photon energy range of 1.2–6.3 eV. A material with a high imaginary part of the dielectric constant absorbs a lot of electromagnetic energy.

Figure 2a shows the optical energy loss function $L(\omega)$ of the three Sn-based 312 MAX phases for the polarization directions $\langle 100 \rangle$ (upper panel) and $\langle 001 \rangle$ (lower panel). This optical parameter describes the amount of energy loss of a fast electron traversing through a material. It correlates inversely with the imaginary part of the dielectric function. In Figure 1d, the imaginary part of the dielectric function shows a broad spectrum for each polarization within the energy range from 0 to 10 eV, while the loss function exhibits no spectrum within this range. This implies that the electron passes through the material with the least energy loss, and the material shows maximum optical conductivity. A large peak due to plasma oscillations occurs in each spectrum of the energy loss function in the energy range of 10–16 eV for both polarizations. The midpoint of this peak can be assigned to a characteristic frequency, which is known as the bulk plasma frequency associated with each compound. The plasma frequencies of Ti_3SnC_2 , Zr_3SnC_2 , and Hf_3SnC_2 are almost the same for the two different polarizations, and they are 12.97, 13.56, and 14.46 eV, respectively.

Figure 2b shows the optical reflectivity of the three MAX compounds under study for the two polarization directions $\langle 100 \rangle$ (upper panel) and $\langle 001 \rangle$ (lower panel). It is an important optical parameter that is related to other optical functions and provides information about the electronic structure of materials. For both polarizations it can be seen that the maximum (about 98%) light is reflected when the photon is incident with lower energy (frequency). High reflectance of light at low frequencies (with low photon

energy) indicates high conductivity and low absorptivity of the studied materials. Then the reflectivity decreases abruptly with increasing photon energy and remains fairly constant in the photon energy range of 0.56–3.54 eV. This range of photon energies includes the visible light range (VLR) of 1.8–3.1 eV. The average reflectivity in the VLR for Ti_3SnC_2 , Zr_3SnC_2 , and Hf_3SnC_2 for the polarization $\langle 100 \rangle$ is 53.6, 51.8, and 51.6%, respectively, while for the polarization $\langle 001 \rangle$ these values are 51.0, 49.2, and 48.0%, respectively. A material should have a reflectivity greater than 44% to be a coating material.³² The studied compounds can be used as coating materials to reduce solar heating. Considering the average for both polarizations, the optical reflectivity is the highest for Ti_3SnC_2 and lowest for Hf_3SnC_2 in the VLR. The reflectivity of the three Sn-based 312 MAX phases reduces when Ti is replaced by Zr and then by Hf from the Ti_3SnC_2 stoichiometry. From the higher energy edge of VLR (2.48–3.31 eV) the reflectivity increases rapidly up to 7.41–9.15 eV for all three phases for the polarization $\langle 100 \rangle$. For the polarization $\langle 001 \rangle$, outside the higher energy range of the VLR, the reflectivity increases rapidly from the photon energy of 3.36–4.24 to 7.31–9.76 eV. At higher photon energies, the bound electrons of the metal atom begin to respond to light rather than simply interacting with the valence band electrons. As a result, Drude's approach then tends to deviate. Depending on the properties of the material, this leads to a decrease in reflectivity. The reflectivity decays fast at a distinctive frequency, known as the material's plasma frequency. The optical anisotropy in reflectivity is slightly pronounced for Ti_3SnC_2 and very negligible for Hf_3SnC_2 .

Figure 2c shows the real part of the refractive index $n(\omega)$, shortly known as the refractive index; the upper panel for the polarization $\langle 100 \rangle$ and the lower panel for the polarization $\langle 001 \rangle$. It is an important optical property of a material, indicating the phase velocity when the electromagnetic waves propagate through the material. The spectra due to $n(\omega)$ for the two different polarizations for each of the Sn-based 312 MAX phases show no significant signs in the anisotropic nature in the optical properties. The large static value (~ 84) of $n(0)$ signifies the metallic nature of the three studied MAX phases. The higher the refractive index, the slower light travels through the medium, the more the light bends, and ultimately—the more efficient the refraction.

Figure 2d exhibits the extinction coefficient $k(\omega)$, the imaginary part of the refractive index, the upper panel for the polarization $\langle 100 \rangle$ and the lower panel for the polarization $\langle 001 \rangle$. It describes the attenuation of electromagnetic waves through a material and determines how intensely the material absorbs radiation at a specific wavelength per mass density or per molar concentration. It is related to the material's conductive properties. A very large value of $k(\omega)$ is assigned to a metallic material, whereas a very small value of $k(\omega)$ is associated with a semiconductor material. On the other hand, dielectric materials are essentially non-conductors with a $k(\omega)$ value of zero. A large static value of $k(0)$ indicates metallic conductivity of the Sn-based 312 MAX phases under study. A slightly anisotropic nature is observed in the visible light region and on both sides of it.

3.2. Lithium Doping. For Li-containing systems in the minimum energy interstitial position in the Sn-based 312 MAX phases, the formation energy, ΔH , upon addition of Li atoms to the system can be determined using the equation given below

$$\Delta H = E(\text{Li-doped system}) - E(\text{pristine system}) - xE(\text{Li})$$

where $E(\text{Li-doped system})$ and $E(\text{pristine system})$ represent the total energy of the system after and before lithium doping, respectively, and x is the number of Li atoms used as the interstitial. In our case, $x = 1$. Likewise, $E(\text{Li})$ is the total energy associated with a single Li atom. To determine the total energy of a Li atom, a body-centered cubic cell of a Li crystal is constructed and then its geometry is relaxed. The obtained total energy is divided by the number of Li atoms within the cell for finding the total energy of a single Li atom. Table 1 lists

Table 1. Formation Energy of Li-Doped Sn-Based 312 MAX Phases and Other Systems

compounds	formation energy (eV)	references
Ti_3SnC_2	2.93	this work, calc.
Zr_3SnC_2	1.66	this work, calc.
Hf_3SnC_2	1.95	this work, calc.
Ti_2SnC	2.83	literature ¹⁷
Zr_2SnC	1.76	literature ¹⁷
Hf_2SnC	2.10	literature ¹⁷
Lu_2SnC	0.36	literature ¹⁷
Nb_2SnC	2.26	literature ¹⁷
V_2SnC	2.80	literature ¹⁷
Sc_2SnC	0.94	literature ¹⁷
Zr_2C	0.30	literature ³⁸
Ti_2C	2.26	literature ⁴⁰
Ti_3C_2	4.40	literature ⁴¹
V_2C	0.96	literature ⁴²
Sc_2C	0.31	literature ⁴³

the formation energy of Li-doped Sn-based 312 MAX phases under consideration, and Figure 3 shows their structures. From Table 1, it is clearly inferred that the Li-doping in the Sn-based 312 MAX phases studied here is endothermic as the formation energy ΔH is greater than 0.5 eV (in the case $x = 1$), signifying structural instability.³⁸ A Zr-based structure has a much lower formation energy compared to Ti- and Hf-based structures, for the reason that the electrostatic repulsion between Zr and Li is weaker than that between Ti and Li and between Hf and Li. Moreover, the formation energies of Li-doped Zr_3SnC_2 and Hf_3SnC_2 are lower than those of their Li-doped 211 MAX phase counterparts Zr_2SnC and Hf_2SnC . The formation energy of Li-doped Ti_3SnC_2 is lower than that of the corresponding 2D MXene Ti_3C_2 , which is an effective light-to-heat conversion material. In a recent paper, it is predicted on the basis of Li ions up taken by pristine MAX phases by reducing their particle size to a submicrometer scale by ultrasonic treatment that there are reasons to believe that many of the MAX phases have great potential to be next-generation anode materials, replacing graphite, tin, or silicon as high-rate electrodes for Li-ion capacitors.³⁹ It is reasonable to believe that it is possible to significantly improve the electrochemical performance of MAX phases by further reducing the particle size and engineering the structure and composition of the materials.³⁹

3.3. Charge Transfer. The amount of charge transfer between atoms of a compound can give a clear picture of the degree of ionicity of that compound. MAX phases are a family of ternary compounds having a mixture of chemical bonding of ionic, covalent and metallic. For this type of compounds the study of charge transfer between atoms is important to

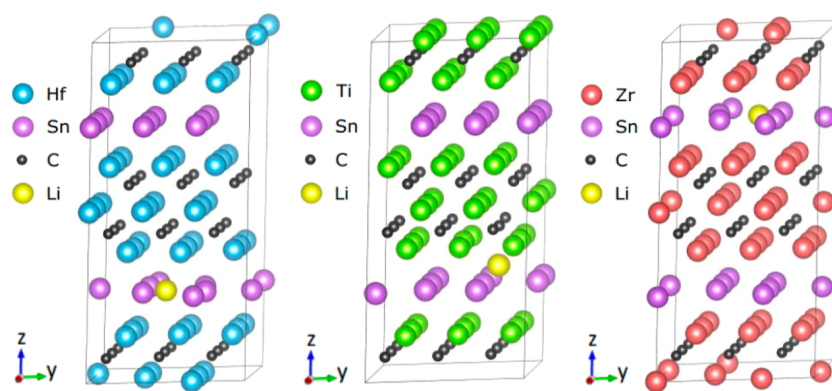


Figure 3. Lithium incorporation in $3 \times 3 \times 1$ supercells of M_3SnC_2 MAX phases.

quantify the level of ionicity in these compounds. Here we used the Mulliken and Bader methods to analyze the charge transfer in Sn-based 312 MAX phases. The Mulliken method gives the Mulliken charge as well as the Hirshfeld charge, while the Bader method gives the Bader charge. Unlike the local basis based Mulliken method, the Bader method uses only a spatial gradient of charge density to analyze the charge density of each atom. According to the Bader technique, the charge density is spread out in space and separated into regions around the atom. These regions, known as Bader regions or volumes, are defined by a 2D surface on which the charge density is a minimum perpendicular to the surface. More precisely, along these surfaces the electron density gradient that is perpendicular to the surfaces, has no component. Usually in molecular systems, the charge density reaches its minimum at a point between the atoms and this point is a natural point of separation of the atoms from each other. A good estimate of the total electronic charge of the corresponding atom is obtained from the charge enclosed within the Bader volume. The charge distribution serves as a useful tool for determining the multipole moments of interacting atoms or molecules. Bader's analysis can also be used to determine the hardness of an atom, which helps measure the cost of removing charge from that atom. Bader charge and Bader volume are shown in Table 2 along with Mulliken and Hirshfeld charges.

The charges in the table are the differences in the number of valence electrons, and these values have been calculated using different techniques for each of the Sn-based 312 MAX

Table 2. Mulliken, Hirshfeld, and Bader Charges (in le) and Bader Volume (in \AA^3)

compounds	elements	Mulliken charge	Hirshfeld charge	Bader charge	Bader volume
Ti_3SnC_2	Ti1	0.67	0.25	0.9929	10.97
	Ti2	0.44	0.16	0.8246	12.96
	Sn	-0.11	0.07	-0.3844	23.23
	C	-0.72	-0.32	-1.1290	10.20
Zr_3SnC_2	Zr1	0.77	0.28	1.1631	15.63
	Zr2	0.45	0.18	0.9220	18.19
	Sn	-0.09	0.04	-0.4294	25.32
	C	-0.79	-0.33	-1.2888	10.74
Hf_3SnC_2	Hf1	0.79	0.27	1.1095	15.04
	Hf2	0.33	0.18	0.8512	17.74
	Sn	0.31	0.00	-0.3879	24.20
	C	-0.87	-0.32	-1.2120	10.21

compounds. The values obtained from the Bader technique and the values obtained from the Mulliken analysis are usually not identical. Among the values in the table, those that are positive indicate the transfer of electrons from the atom and those that are negative indicate the acceptance of electrons by the atom. In the results obtained by the Bader method, only the M-atom transfers its charge to both the Sn and C atoms. According to the results obtained from the Mulliken method, in the case of Hf_3SnC_2 , the M-atom along with the Sn-atom participates in charge transfer, and in this system, only the C atom accepts charge. Otherwise, in the case of Hirshfeld charge, the M-atom of Ti_3SnC_2 and Zr_3SnC_2 as well as the Sn atom also participate in charge transfer, and in these systems, only the C atom accepts charge. The Sn atom of Hf_3SnC_2 plays a neutral role, i.e., it does not play any role in charge acceptance and transfer. Bader charge has a higher magnitude than Mulliken and Hirshfeld charges. Although Mulliken charge analysis is widely used, Bader charge analysis is more acceptable than Mulliken and Hirshfeld charge analysis because it is based on a stronger theoretical foundation. In relation to Bader analysis, maximum charge transfer takes place between atoms of Zr_3SnC_2 and minimum charge transfer comes to pass between atoms of Ti_3SnC_2 .

3.4. Electron Localization Function. We calculate the ELF, which was introduced by Becke and Edgcombe⁴⁴ as a dimensionless indicator of electron localization. It is related to the electron probability density of a same-spin electron pair and ranges between 0 and 1. It provides additional information on the strength and location of the bonds. Regions that demonstrate high ELF values (near unity) are regions with high electron localization, whereas lower values (approaching 0.5) correspond to lower localization. An ELF at 0.5 corresponds to full delocalization, similar to that of an electron gas, while lower values than that exist in areas where there is minimal concentration of electron density.^{45,46}

In Figure 4, the calculated ELF maps for the [001] and [100] planes are shown. Also, the [011] surface has been plotted in Figure 5 in order to visualize the area around the carbon atoms. Additional 3D maps are shown in Figure 6. The regions around the metal ions and the carbon cores show higher electron localization, with typical circular domains (characteristic of the electron shells). The bonds between carbon and metal ions are expected to be strongly localized. This is in agreement with the calculated ELF maps which show a combination of highly localized regions surrounded by low localization (blue–red areas), whereas in the case of Sn and metal (yellow–green areas), there is smaller localization that is

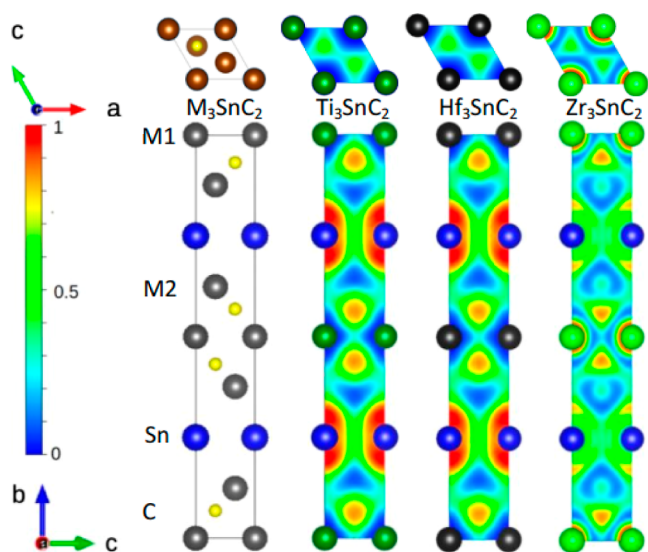


Figure 4. ELF maps for the [001] (top) and [100] (bottom) planes for the M_3SnC_2 phases.

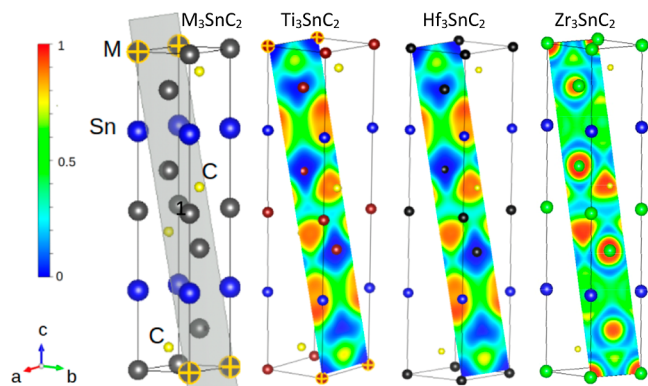


Figure 5. ELF maps along the [011] plane for three M_3SnC_2 phases.

interpreted as a weaker bond. Differences among the different M_3SnC_2 structures are related to the core radius and the number of electron shells. However, the ELF method should be used with caution when applied to transition metal atoms. For transition metal atoms, the ELF displays very low values that are always lower than 0.5, as shown in Figure 6 (for the isosurface $n = 0.5$).⁴⁴

4. CONCLUSIONS

In summary, DFT was employed for the first time to comprehensively investigate the optical response, Li-doping and charge transfer in Sn-based 312 M_3SnC_2 MAX phases with ELF. The spectral characteristics are slightly different for the two different polarization directions of incident light, and the peak height is mostly slightly higher for the polarization $\langle 001 \rangle$. The highest peak due to light absorption shifts toward higher energy when the M-element Ti is replaced by Zr and then by Hf. Above photon energies of 6.1 and 5.3 eV, the absorption rates of light for Hf_3SnC_2 are highest for the polarizations $\langle 100 \rangle$ and $\langle 001 \rangle$, respectively. A sharp peak in the optical conductivity spectra due to both polarizations in the region near zero frequency (energy) specifies the metallic conductivity of the M_3SnC_2 MAX phases. The large negative values of $\epsilon_1(\omega)$ in the low energy part of each spectrum reveal

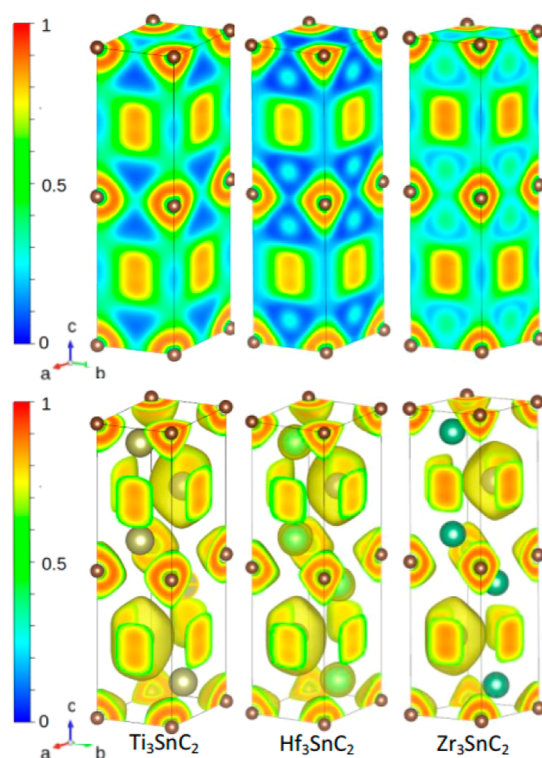


Figure 6. 3D ELF maps with $n = 0.0$ (upper panels) and $n = 0.5$ (lower panels) for the three M_3SnC_2 MAX phases.

the Drude-like behavior of the Sn-based 312 MAX phases. Again, the real part $\epsilon_1(\omega)$ goes from negative to zero, indicating the metallic nature of these MAX compounds. The non-zero value of $\epsilon_1(\omega)$ indicates the possibility of large availability of free charge carriers in these metallic systems. A large peak due to plasma oscillations occurs in each spectrum of the energy loss function and the plasma frequencies of Ti_3SnC_2 , Zr_3SnC_2 , and Hf_3SnC_2 are almost the same for the two different polarizations, and they are 12.97, 13.56, and 14.46 eV, respectively. The average reflectivity for the three MAX phases under study is sufficient for them to be a coating material to reduce solar heating. The large static values of n and k indicate the metallic conductivity of these compounds. A slight optical anisotropy is visible in the spectra due to different optical parameters in some energy ranges of the incident photons. The formation energies of Li-doped Zr_3SnC_2 and Hf_3SnC_2 are lower than those of their Li-doped 211 MAX phase counterparts Zr_2SnC and Hf_2SnC . The formation energy of Li-doped Ti_3SnC_2 is lower than that of the corresponding 2D MXene Ti_3C_2 , which is a promising photothermal material. Bader charge is higher in magnitude than Mulliken and Hirschfeld charges. According to Bader analysis, maximum charge transfer occurs in Zr_3SnC_2 and minimum charge transfer occurs in Ti_3SnC_2 . ELF reveals that the bonds between carbon and metal ions are strongly localized, whereas in the case of Sn and metal ions, there is smaller localization that is interpreted as a weaker bond.

AUTHOR INFORMATION

Corresponding Author

Md. Abdul Hadi – Department of Physics, University of Rajshahi, Rajshahi 6205, Bangladesh; Department of Physics, Nazipur Government College, Naogaon 6540,

Bangladesh; orcid.org/0000-0001-8096-1677;
Email: hadipab@gmail.com

Authors

Nicolas Kelaidis – Institute of Nanoscience and Nanotechnology (INN), National Center for Scientific Research 'Demokritos', Athens 15310, Greece; Theoretical and Physical Chemistry Institute, National Hellenic Research Foundation, Athens GR-11635, Greece

Stavros-Richard G. Christopoulos – Department of Computer Science, School of Computing and Engineering, University of Huddersfield, Huddersfield HD4 6DJ, U.K.; Centre for Computational Science and Mathematical Modelling, Coventry University, Coventry CV1 2TU, U.K.; orcid.org/0000-0002-8468-2998

Alexander Chroneos – Department of Electrical and Computer Engineering, University of Thessaly, Volos 38221, Greece; Department of Materials, Imperial College, London SW7 2AZ, U.K.

Saleh Hasan Naqib – Department of Physics, University of Rajshahi, Rajshahi 6205, Bangladesh

A. K. M. Azharul Islam – Department of Physics, University of Rajshahi, Rajshahi 6205, Bangladesh; International Islamic University Chittagong, Chittagong 4318, Bangladesh

Complete contact information is available at:

<https://pubs.acs.org/10.1021/acsomega.3c03645>

Notes

The authors declare no competing financial interest.

ACKNOWLEDGMENTS

The authors wish to acknowledge the High-Performance Computing (HPC) facility at Coventry University, Priory Street, Coventry CV1 5FB, UK, and the Institute of Nanoscience and Nanotechnology (INN), National Center for Scientific Research 'Demokritos', 15310 Agia Paraskevi, Athens, Greece, for providing the computational facility to calculate the lithiation and ELF in the $M_3\text{SnC}_2$ MAX phase.

REFERENCES

- (1) Hadi, M. A. Superconducting phases in a remarkable class of metallic ceramics. *J. Phys. Chem. Solids* **2020**, *138*, 109275.
- (2) Hadi, M. A.; Ahmed, I.; Ali, M. A.; Hossain, M. M.; Nasir, M. T.; Ali, M. L.; Naqib, S. H.; Islam, A. K. M. A. A comparative DFT exploration on M- and A-site double transition metal MAX phase, Ti_3ZnC_2 . *Open Ceram.* **2022**, *12*, 100308.
- (3) Li, Y.; Liang, J.; Ding, H.; Lu, J.; Mu, X.; Yan, P.; Zhang, X.; Chen, K.; Li, M.; Persson, P. O. Å.; Hultman, L.; Eklund, P.; Du, S.; Yang, H.; Chai, Z.; Huang, Q. Near-room temperature ferromagnetic behavior of single-atom-thick 2D iron in nanolaminated ternary MAX phases. *Appl. Phys. Rev.* **2021**, *8*, 031418.
- (4) Barsoum, M. W. The $M_{N+1}AX_N$ Phases: A New Class of Solids; Thermodynamically Stable Nanolaminates. *Prog. Solid State Chem.* **2000**, *28*, 201–281.
- (5) Hadi, M. A.; Christopoulos, S.-R. G.; Chroneos, A.; Naqib, S. H.; Islam, A. K. M. A. DFT insights into the electronic structure, mechanical behaviour, lattice dynamics and defect processes in the first Sc-based MAX phase Sc_2SnC . *Sci. Rep.* **2022**, *12*, 14037.
- (6) Zapata-Solvas, E.; Hadi, M. A.; Horlait, D.; Parfitt, D. C.; Thibaud, A.; Chroneos, A.; Lee, W. E. Synthesis and physical properties of $(\text{Zr}_{1-x}\text{Ti}_x)_3\text{AlC}_2$ MAX phases. *J. Am. Ceram. Soc.* **2017**, *100*, 3393–3401.
- (7) Mo, Y.; Rulis, P.; Ching, W. Y. Electronic structure and optical conductivities of 20 MAX-phase compounds. *Phys. Rev. B: Condens. Matter Mater. Phys.* **2012**, *86*, 165122.
- (8) Nappé, J. C.; Grosseau, Ph.; Audubert, F.; Guillot, B.; Beauvy, M.; Benabdesselam, M.; Monnet, I. Damages induced by heavy ions in titanium silicon carbide: Effects of nuclear and electronic interactions at room temperature. *J. Nucl. Mater.* **2009**, *385*, 304–307.
- (9) Meng, F.; Chaffron, L.; Zhou, Y. Synthesis of Ti_3SiC_2 by high energy ball milling and reactive sintering from Ti, Si, and C elements. *J. Nucl. Mater.* **2009**, *386–388*, 647–649.
- (10) Wang, J.; Zhou, Y. Recent Progress in Theoretical Prediction, Preparation, and Characterization of Layered Ternary Transition-Metal Carbides. *Annu. Rev. Mater. Res.* **2009**, *39*, 415–443.
- (11) Eklund, P.; Beckers, M.; Jansson, U.; Högborg, H.; Hultman, L. The $M_{n+1}AX_n$ phases: Materials science and thin-film processing. *Thin Solid Films* **2010**, *518*, 1851–1878.
- (12) Tallman, D. J.; He, L.; Gan, J.; Caspi, E. N.; Hoffman, E. N.; Barsoum, M. W. Effects of neutron irradiation of Ti_3SiC_2 and Ti_3AlC_2 in the 121–1085° C temperature range. *J. Nucl. Mater.* **2017**, *484*, 120–134.
- (13) Shuck, C. E.; Gogotsi, Y. MXenes: A Tunable Family of 2D Carbides and Nitrides with Diverse Applications. *Mater. Matters* **2020**, *15*, 3.
- (14) Zhao, S.; Dall'Agnesse, Y.; Chu, X.; Zhao, X.; Gogotsi, Y.; Gao, Y. Electrochemical Interaction of Sn-Containing MAX phase (Nb_2SnC) with Li-Ions. *ACS Energy Lett.* **2019**, *4*, 2452–2457.
- (15) Xu, Q.; Zhou, Y.; Zhang, H.; Jiang, A.; Tao, Q.; Lu, J.; Rosén, J.; Niu, Y.; Grasso, S.; Hu, C. Theoretical prediction, synthesis, and crystal structure determination of new MAX phase compound V_2SnC . *J. Adv. Ceram.* **2020**, *9*, 481–492.
- (16) Li, Y.; Qin, Y.; Chen, K.; Chen, L.; Zhang, X.; Ding, H.; Li, M.; Zhang, Y.; Du, S.; Chai, Z.; Huang, Q. Molten Salt Synthesis of Nanolaminated Sc_2SnC MAX Phase. *J. Inorg. Mater.* **2021**, *36*, 773.
- (17) Hadi, M. A.; Kelaidis, N.; Filippatos, P. P.; Christopoulos, S.-R. G.; Chroneos, A.; Naqib, S. H.; Islam, A. K. M. A. Optical response, lithiation and charge transfer in Sn-based 211 MAX phases with electron localization function. *J. Mater. Res. Technol.* **2022**, *18*, 2470–2479.
- (18) Hadi, M. A.; Dahlqvist, M.; Christopoulos, S.-R. G.; Naqib, S. H.; Chroneos, A.; Islam, A. K. M. A. Chemically stable new MAX phase V_2SnC : a damage and radiation tolerant TBC material. *RSC Adv.* **2020**, *10*, 43783–43798.
- (19) Hadi, M. A.; Kelaidis, N.; Naqib, S. H.; Chroneos, A.; Islam, A. K. M. A. Electronic structures, bonding natures and defect processes in Sn-based 211 MAX phases. *Comput. Mater. Sci.* **2019**, *168*, 203–212.
- (20) Hadi, M.; Kelaidis, N.; Naqib, S. H.; Chroneos, A.; Islam, A. K. M. A. Mechanical behaviors, lattice thermal conductivity and vibrational properties of a new MAX phase Lu_2SnC . *J. Phys. Chem. Solids* **2019**, *129*, 162–171.
- (21) Dubois, S.; Cabioch, T.; Chartier, P.; Gauthier, V.; Jaouen, M. A New Ternary Nanolaminated Carbide: Ti_3SnC_2 . *J. Am. Ceram. Soc.* **2007**, *90*, 2642–2644.
- (22) Lapauw, T.; Tunca, B.; Cabioch, T.; Vleugels, J.; Lambrinou, K. Reactive spark plasma sintering of Ti_3SnC_2 , Zr_3SnC_2 and Hf_3SnC_2 using Fe, Co or Ni additives. *J. Eur. Ceram. Soc.* **2017**, *37*, 4539–4545.
- (23) Hadi, M. A.; Christopoulos, S.-R. G.; Naqib, S. H.; Chroneos, A.; Fitzpatrick, M. E.; Islam, A. K. M. A. Physical properties and defect processes of $M_3\text{SnC}_2$ ($M = \text{Ti}, \text{Zr}, \text{Hf}$) MAX phases: Effect of M-elements. *J. Alloys Compd.* **2018**, *748*, 804–813.
- (24) Clark, S. J.; Segall, M. D.; Pickard, C. J.; Hasnip, P. J.; Probert, M. I. J.; Refson, K.; Payne, M. C. First principles methods using CASTEP. *Z. Kristallogr.* **2005**, *220*, 567–570.
- (25) Perdew, J. P.; Burke, K.; Ernzerhof, M. Generalized Gradient Approximation Made Simple. *Phys. Rev. Lett.* **1996**, *77*, 3865–3868.
- (26) Hadi, M. A.; Kelaidis, N.; Naqib, S. H.; Islam, A.; Chroneos, A.; Vovk, R. Insights into the physical properties of a new 211 MAX phase Nb_2CuC . *J. Phys. Chem. Solids* **2021**, *149*, 109759.
- (27) Vanderbilt, D. Soft self-consistent pseudopotentials in a generalized eigenvalue formalism. *Phys. Rev. B: Condens. Matter Mater. Phys.* **1990**, *41*, 7892–7895.

- (28) Monkhorst, H. J.; Pack, J. D. Special points for Brillouin-zone integrations. *Phys. Rev. B: Solid State* **1976**, *13*, 5188–5192.
- (29) Fischer, T. H.; Almlöf, J. General methods for geometry and wave function optimization. *J. Phys. Chem.* **1992**, *96*, 9768–9774.
- (30) Kresse, G.; Furthmüller, J. Efficient iterative schemes for ab initio total-energy calculations using a plane-wave basis set. *Phys. Rev. B: Condens. Matter Mater. Phys.* **1996**, *54*, 11169–11186.
- (31) He, X.; Bai, Y.; Chen, Y.; Zhu, C.; Li, M.; Barsoum, M. W. Phase Stability, Electronic Structure, Compressibility, Elastic and Optical Properties of a Newly Discovered Ti_3SnC_2 : A First-Principle Study. *J. Am. Ceram. Soc.* **2011**, *94*, 3907–3914.
- (32) Li, S.; Ahuja, R.; Barsoum, M. W.; Jena, P.; Johansson, B. Optical properties of Ti_3SiC_2 and Ti_4AlN_3 . *Appl. Phys. Lett.* **2008**, *92*, 221907.
- (33) Li, X.; Cui, H.; Zhang, R. First-principles study of the electronic and optical properties of a new metallic MoAlB. *Sci. Rep.* **2016**, *6*, 39790.
- (34) Hadi, M. A.; Vovk, R. V.; Chroneos, A. Physical properties of the recently discovered $\text{Zr}_2(\text{Al}_{1-x}\text{Bi}_x)\text{C}$ MAX phases. *J. Mater. Sci.: Mater. Electron.* **2016**, *27*, 11925–11933.
- (35) Hadi, M. A.; Roknuzzaman, M.; Nasir, M.; Monira, U.; Naqib, S. H.; Chroneos, A.; Islam, A. K. M. A.; Alarco, J. A.; Ostrikov, K. Effects of Al substitution by Si in Ti_3AlC_2 nanolaminate. *Sci. Rep.* **2021**, *11*, 3410.
- (36) Mitro, S. K.; Hadi, M. A.; Parvin, F.; Majumder, R.; Naqib, S. H.; Islama, A. Effect of boron incorporation into the carbon-site in Nb_2SC MAX phase: Insights from DFT. *J. Mater. Res. Technol.* **2021**, *11*, 1969–1981.
- (37) Roknuzzaman, M.; Hadi, M. A.; Abden, M. J.; Nasir, M. T.; Islam, A. K. M. A.; Ali, M. S.; Ostrikov, K.; Naqib, S. H. Physical properties of predicted Ti_2CdN versus existing Ti_2CdC MAX phase: An ab initio study. *Comput. Mater. Sci.* **2016**, *113*, 148–153.
- (38) Zhu, J.; Chroneos, A.; Wang, L.; Rao, F.; Schwingenschlögl, U. Stress-enhanced lithiation in MAX compounds for battery applications. *Appl. Mater. Today* **2017**, *9*, 192–195.
- (39) Xu, J.; Zhao, M.-Q.; Wang, Y.; Yao, W.; Chen, C.; Anasori, B.; Sarycheva, A.; Ren, C. E.; Mathis, T.; Gomes, L.; Zhenghua, L.; Gogotsi, Y. Demonstration of Li-Ion Capacity of MAX Phases. *ACS Energy Lett.* **2016**, *1*, 1094–1099.
- (40) Wan, Q.; Li, S.; Liu, J. First-Principle Study of Li-Ion Storage of Functionalized Ti_2C Monolayer with Vacancies. *ACS Appl. Mater. Interfaces* **2018**, *10*, 6369–6377.
- (41) Er, D.; Li, J.; Naguib, M.; Gogotsi, Y.; Shenoy, V. B. Ti_3C_2 MXene as a High Capacity Electrode Material for Metal (Li, Na, K, Ca) Ion Batteries. *ACS Appl. Mater. Interfaces* **2014**, *6*, 11173–11179.
- (42) Li, Y.-M.; Guo, Y.-L.; Jiao, Z.-Y. The effect of S-functionalized and vacancies on V_2C MXenes as anode materials for Na-ion and Li-ion batteries. *Curr. Appl. Phys.* **2020**, *20*, 310–319.
- (43) Lv, X.; Wei, W.; Sun, Q.; Yu, L.; Huang, B.; Dai, Y. Sc_2C as a Promising Anode Material with High Mobility and Capacity: A First-Principles Study. *Chem. Phys. Chem.* **2017**, *18*, 1627–1634.
- (44) Becke, A. D.; Edgecombe, K. E. A simple measure of electron localization in atomic and molecular systems. *J. Chem. Phys.* **1990**, *92*, 5397–5403.
- (45) Fuentealba, P.; Chamorro, E.; Santos, J. C. Understanding and using the electron localization function. *Theoretical Aspects of Chemical Reactivity*; Elsevier, 2007; Chapter 5.
- (46) Burdett, J. K.; McCormick, T. A. Electron Localization in Molecules and Solids: The Meaning of ELF. *J. Phys. Chem. A* **1998**, *102*, 6366–6372.